



# Experimental and computational investigation of vertical downflow condensation



Hyoungsoon Lee, Chirag R. Kharangate, Nikhin Mascarenhas, Ilchung Park, Issam Mudawar<sup>\*</sup>

Purdue University Boiling and Two-Phase Flow Laboratory (PU-BTFL), Mechanical Engineering Building, 585 Purdue Mall, West Lafayette, IN 47907-2088, USA

## ARTICLE INFO

### Article history:

Received 1 July 2014

Received in revised form 10 February 2015

Accepted 12 February 2015

### Keywords:

Condensation

Computational two-phase flow

Annular flow

Vertical downflow

## ABSTRACT

This explores downflow condensation in a circular tube both experimentally and computationally using FC-72 as a working fluid. A highly instrumented condensation module is used to map detailed axial variations of both wall heat flux and wall temperature, which are used to determine axial variations of the condensation heat transfer coefficient. The experimental results are compared to predictions of a two-dimensional axisymmetric computational model using FLUENT. The study provides detailed construction of the model, including choice of interfacial phase change sub-model, numerical methods, and convergence criteria. The model is shown to yield good prediction of the heat transfer coefficient. The computed temperature profiles exhibit unusual shape, with steep gradient near the annular liquid film interface as well as near the wall, and a mild gradient in between. This shape is shown to be closely related to the shape of the eddy diffusivity profile. These findings point to the need for future, more sophisticated measurements of liquid film thickness, and both velocity and temperature profiles, to both validate and refine two-phase computational models.

© 2015 Elsevier Ltd. All rights reserved.

## 1. Introduction

### 1.1. Importance of predictive tools for two-phase cooling system design

Two-phase cooling systems have gained significant popularity in recent years due to an urgent need to tackle unprecedented heat dissipation challenges in commercial, aerospace and defense electronics. Heat dissipation rates at the device and system levels in these applications are no longer manageable with single-phase cooling systems. Therefore, more aggressive two-phase cooling solutions are being sought, using a variety of configurations, such as pool [1–3], mini/micro-channel [4–7], jet [8–10] and spray [11,12], as well as hybrid configurations combining the benefits of two or more of these configurations [13,14]. These two-phase cooling solutions have already yielded as high as 1127 W/cm<sup>2</sup> using dielectric coolants [15] and 27,600 W/cm<sup>2</sup> using water [16,17].

A complete two-phase cooling system requires an effective means for rejecting the heat absorbed from the electronics to the

ambient, and this is generally achieved with the aid of a high performance condenser. Unfortunately, recent studies concerning the development of two-phase cooling solutions have focused mostly on the heat acquisition by boiling, and to a far lesser degree on ultimate rejection of the heat by condensation. Clearly, a better understanding of the thermal performance of high performance condensers is needed to achieve a more complete methodology for cooling system design. Recent findings concerning fluid flow and heat transfer mechanisms of condensation are available in Refs. [18–20].

While empirical formulations constitute the most popular means for predicting transport behavior in condensers [21–23], these formulations are limited by working fluids, geometries, and operating conditions of the databases upon which they are based. To achieve more universal predictive tools, there is a desire to develop both theoretical and computational techniques. Theoretical models are based mostly on the application of mass, momentum and energy conservation laws to control volumes encompassing the liquid and vapor phases or the entire flow [24]. These models have been especially effective for annular condensation, but far less so for slug flow and bubbly flow. But even for annular flow, there are major modeling challenges stemming from a lack of ability to model interfacial waves and the influence of the interface on turbulence in both the liquid film and vapor core [24–26].

<sup>\*</sup> Corresponding author. Tel.: +1 (765) 494 5705; fax: +1 (765) 494 0539.

E-mail address: [mudawar@ecn.purdue.edu](mailto:mudawar@ecn.purdue.edu) (I. Mudawar).

URL: <http://engineering.purdue.edu/BTFL> (I. Mudawar).

## Nomenclature

$c_p$	specific heat at constant pressure
$c$	mesh (cell) size
$D$	diameter
$E$	energy per unit mass
$F$	force
$G$	mass velocity
$g$	gravitational acceleration
$H$	step function
$h$	heat transfer coefficient
$h_{fg}$	latent heat of vaporization
$I$	turbulence intensity
$J_e^h$	heat flux from wall to interface in Schrage model
$k$	thermal conductivity
$L$	length
$M$	molecular weight
$\dot{m}''$	mass flux
$n$	number of cells
$\vec{n}$	unit vector normal to interface
$P$	pressure
$Pr$	Prandtl number
$Pr_T$	turbulent Prandtl number
$Q$	energy source term
$q''$	heat flux
$R$	universal gas constant (8.314 J/mol K)
$r$	radial coordinate
$Re$	Reynolds number
$r_i$	mass transfer intensity factor
$S$	volumetric mass source
$T$	temperature
$t$	time
$t^+$	dimensionless time
$U$	mean inlet vapor velocity
$u$	velocity
$u'$	fluctuating component of velocity
$u^*$	friction velocity $\sqrt{\tau_{wall}/\rho_f}$
$V$	volume
$x_e$	thermodynamic equilibrium quality

$y$	distance perpendicular to wall
$y^+$	dimensionless distance perpendicular to wall
$z$	stream-wise coordinate
$z_0$	location where $x_e = 1$

### Greek symbols

$\alpha$	volume fraction, void fraction
$\gamma$	accommodation coefficient in Schrage model
$\delta$	liquid film thickness
$\varepsilon_m$	eddy momentum diffusivity
$\eta_e$	evaporation heat transfer coefficient in Schrage model
$\mu$	dynamic viscosity
$\nu$	kinematic viscosity
$\rho$	density
$\sigma$	surface tension
$\tau$	shear stress
$\phi$	level set function
$\psi$	generic property

### Superscript

–	average component
---	-------------------

### Subscripts

$c$	condensation
$D$	diameter
$e$	evaporation; thermodynamic equilibrium
$eff$	effective
$exp$	experimental
$f$	liquid
$g$	vapor
$i$	initial; interfacial
$in$	inlet
$sat$	saturated
$w$	water
$wall$	wall

## 1.2. Application of commercial software and numerical methods to two-phase systems

The limitations of empirical formulations and theoretical models point to the need for computational tools that can tackle interfacial waviness, turbulence structure, and different condensation flow patterns. Computational tools have been quite effective in simulating complex turbulent single-phase systems, showing good agreement with experimental data. And computation efforts have benefitted greatly from both the developments in CPU processing speed and availability of commercial CFD software such as ANSYS FLUENT, OpenFOAM, FLOW-3D and COMSOL. Increasingly, these software packages have been able to combine various numerical techniques to enhance prediction accuracy. Aside from the ability to tackle complicated geometries, computational tools can significantly reduce cost, especially for efforts where extensive testing is cost prohibitive such as microgravity experiments [27]. However, the ability of commercial software to accurately predict complex two-phase flows is questionable, which is why many researchers are making persistent efforts in pursuit of improved accuracy.

Numerical approaches to modeling two-phase systems have been studied quite thoroughly and several types of approaches have been developed for this purpose. These approaches can be

categorized into three different types: (1) Lagrangian, (2) Eulerian and (3) Eulerian–Lagrangian.

Smoothed-Particle Hydrodynamics (SPH) [28,29] and Multiphase Particle-in-Cell (MP-PIC) [30] methods are based on the Lagrangian approach. These methods provide a high level of accuracy at the interface and allow interfacial boundary conditions to be easily applied because they can tackle individual fluid particles and determine how these particles behave in motion. However, Lagrangian methods are limited to simple cases due to the complexity of applying complicated grid topologies. Therefore, as the demand for solving complex situations increases, methods following Eulerian perspectives have gained more popularity, given their simplicity, feasibility of tackling multiple interfaces (e.g., multiple bubbles), and relative ease of implementation into commercial CFD software.

Level-Set Method (LSM) [31] and Volume-of-Fluid (VOF) method [32] are two representative examples based on the Eulerian perspective. Developed by Osher and Sethian [31], LSM tracks the interface by a smooth function  $\phi$ , where  $\phi = 0$  at the interface, which is called the zero level set, and is positive for one phase and negative for the other. In this method, interfacial topologies such as curvatures and sharp interfaces can be easily captured. However, this method suffers an inability to tackle mass conservation, as it results in loss of mass when solving the

advection equation. Therefore, many researchers employ a separate method such as the fractional-step method or projection method to achieve mass conservation in LSM [33]. VOF is a numerical method for tracking an interface based on the phase volume fraction,  $\alpha$ , of each phase, which has a value between 0 and 1. The sum of volume fractions of vapor and liquid in a cell is equal to unity, and the properties of each cell are determined as follows:

$$\psi = \sum_i \alpha_i \psi_i, \quad (1)$$

where  $\psi$  can be any property such as density or viscosity. This method can be solved without the mass loss, however, it compromises estimation of the interface topology compared to LSM. This prompted researchers to combine different methods to compensate for the disadvantages of individual methods in tackling two-phase problems. Coupled Level Set/Volume of Fluid (CLSVOF) method [34–36] is one of the most actively researched combined methods, and is based on LSM, with the VOF used to conserve mass when the interface is advected. Unverdi and Tryggvason [37] and Tryggvason et al. [38] used the combined Eulerian–Lagrangian perspective, which is called the front tracking method. This method utilizes a fixed grid method with a moving grid at the interface to capitalize on the advantages of both Eulerian and Lagrangian systems.

### 1.3. Phase change models

The phase change process also has been tackled in numerical methods separately using different types of models. The sharp interface model has been used since the early 1990s when numerical simulation of phase change was initially attempted. The sharp interface model is based on the Rankine–Hugoniot jump condition [39] for energy conservation, where all the heat transferred at the interface is assumed to be consumed by latent heat due to phase change. If micro-scale mass transfer can be neglected and interfacial temperature is assumed to equal the saturation temperature, mass transfer rate can be determined from energy conservation according to the relation

$$q_i'' = -k_{eff} \nabla T_i \cdot \vec{n} = \dot{m}'' h_{fg}, \quad (2)$$

where  $\dot{m}''$  [kg/m<sup>2</sup> s] is the mass flux due to phase change at the interface. The volumetric mass source term,  $S$  [kg/m<sup>3</sup> s], for the individual phases can be determined as follows,

$$S_g = -S_f = \dot{m}'' |\nabla \alpha_g| = \frac{k_{eff} (\nabla \alpha \cdot \nabla T)}{h_{fg}}, \quad (3)$$

where  $k_{eff}$  is the effective thermal conductivity, which can be determined from the volume fractions and thermal conductivities of the vapor and liquid.

Son and Dhir [33], Gibou et al. [39] and Bazdidi-Tehrani and Zaman [40] adopted the sharp interface model using the LSM to simulate pool boiling. Ganapathy et al. [41] used the sharp interface model with the VOF method to simulate condensation in micro-channels. Sun et al. [42] proposed the following simplified equation based on the assumption of linear distribution of  $T_f$  near the interface and negligible heat conduction in the saturated vapor phase ( $k_g = 0$ ).

$$S_g = -S_f = \frac{2k_f (\nabla \alpha_f \cdot \nabla T)}{h_{fg}}. \quad (4)$$

They recommended that the effective thermal conductivity,  $k_{eff}$ , in Eq. (3), which is determined from the conductivities of vapor and liquid, be replaced by twice the liquid conductivity, which they justified by the observation that bubble growth in superheated liquid is not related to the vapor conductivity.

Schrage [43] proposed a different type of phase change model based on the Hertz–Knudsen equation [44], with the interfacial jump in the temperature and pressure  $T_{sat}(P_f) = T_f \neq T_{sat}(P_g) = T_g$ . Mass flux at the interface was determined from mass conservation at the interface between the mass fluxes from liquid to vapor and from vapor to liquid.

$$\dot{m}'' = \frac{2}{2 - \gamma_c} \sqrt{\frac{M}{2\pi R}} \left[ \gamma_c \frac{P_g}{\sqrt{T_g}} - \gamma_e \frac{P_f}{\sqrt{T_f}} \right], \quad (5)$$

where  $R = 8.314$  J/mol K is the universal gas constant,  $\gamma$  the fraction of molecules transferred from one phase to the other during phase change, and  $1 - \gamma$  the fraction reflected. The subscripts  $c$  and  $e$  in Eq. (5) refer to condensation and evaporation, respectively;  $\gamma_e = 1$  and  $\gamma_c = 1$  represent complete evaporation and complete condensation, respectively [45]. Many investigators use equal values of  $\gamma_c$  and  $\gamma_e$  by setting  $\gamma_c = \gamma_e = \gamma$  in phase change simulations and referred to  $\gamma$  as the accommodation coefficient. Marek and Straub [45] determined  $\gamma$  based on published data. They recommended  $\gamma = 0.1$ – $1$  for dynamically renewing water surfaces such as jets or moving films, and  $\gamma < 0.1$  for stagnant surfaces. Hardt and Wondra [46] set  $\gamma = 1$  for film boiling, and Magnini et al. [47] also set  $\gamma = 1$  for laminar flow boiling based on a recommendation by Rose [48]. On the other hand, Kartuzova and Kassemi [49] used a relatively low value of  $\gamma = 0.01$  in their simulation of ventless pressurization of a cryogenic storage tank.

Tanasawa [50] simplified Eq. (5) by assuming the interfacial temperature is equal to  $T_{sat}$ , and the heat flux linearly dependant on the temperature jump between the interface and the vapor. Their modified model for evaporation situations is expressed as

$$\dot{m}'' = \frac{2\gamma}{2 - \gamma} \sqrt{\frac{M}{2\pi R}} \frac{\rho_g h_{fg} (T - T_{sat})}{T_{sat}^{3/2}}, \quad (6)$$

where  $T_{sat}$  is based on local pressure,  $P$ , and the volumetric mass source term is determined from

$$S_g = -S_f = \dot{m}'' |\nabla \alpha_g|. \quad (7)$$

Lee [51] derived a third type of phase change model, which is the most widely used for simulating phase change processes, especially condensation. This model is based on the assumption that mass is transferred at a constant pressure and a quasi thermo-equilibrium state, and obtained from the following equations:

$$S_g = -S_f = r_i \alpha_g \rho_g \frac{(T - T_{sat})}{T_{sat}} \quad \text{for condensation } (T < T_{sat}), \quad (8a)$$

and

$$S_g = -S_f = r_i \alpha_f \rho_f \frac{(T - T_{sat})}{T_{sat}} \quad \text{for evaporation } (T > T_{sat}), \quad (8b)$$

where  $r_i$  is an empirical coefficient called the *mass transfer intensity factor* [42] and has the units of  $s^{-1}$ . Researchers have used a very wide range of  $r_i$  values, which seem to change not only with the flow geometry and flow conditions, but mesh size and time step as well. Wu et al. [52] set  $r_i = 0.1$  in their simulations of flow boiling in serpentine tubes. The same value of  $r_i = 0.1$  was used by De Schepper et al. [53] in simulating flow boiling in a hydrocarbon feedstock, and by Alizadehdakhel et al. [54] for investigation of evaporation and condensation in a thermosyphon. Yang et al. [55] set  $r_i = 100$  in order to numerically maintain the interfacial temperature,  $T_i$ , within  $T_{sat} \pm 1$  K. They pointed out that very small values of  $r_i$  cause the interfacial temperature to deviate from the saturated temperature. Fang et al. [56] also set  $r_i = 100$ , and, like Yang et al., concluded that very small values of  $r_i$  cause significant deviation of  $T_i$  from  $T_{sat}$ , and increasing  $r_i$  helps maintain  $T_i$  close to  $T_{sat}$ ; they also pointed out that extremely large values of  $r_i$  cause

**Table 1**  
Summary of computational phase change literature.

Author(s)	System	Model	Discretization scheme & mesh	Remarks
<i>Sharp interface model</i> Son and Dhir (1998) [33]	Horizontal film boiling	Sharp Interface model: $\dot{m}'' = \frac{-k_{eff} \nabla T}{h_{fg}}$ where $k_{eff}^{-1} = k_g^{-1} + (k_f^{-1} - k_g^{-1})H$ BC: $T_{wall} = \text{constant}$	Line-by-line TriDiagonal Method Algorithm (TDMA) with multigrid method, Gauss–Seidel method	LSM, 2D, axisymmetric, laminar, water
Bazdidi-Tehrani and Zaman (2002) [40]	Vertical film boiling	Sharp interface model: $\dot{m}'' = \frac{-k_{eff} \nabla T}{h_{fg}}$ BC: $T_{wall} = \text{constant}$	Line-by-line TDMA with multigrid method, Gauss–Seidel method, fully implicit scheme (diffusion), 1st explicit method (convection source), rectangular mesh (256 × 128)	LSM, 2D, planner, laminar, $t^* = 0.01$
Gibou et al. (2007) [39]	Film boiling	Sharp interface model: $\dot{m}'' = \frac{-k_{eff} \nabla T}{h_{fg}}$ BC: imposed interfacial boundary for $T$ , $V$ and $\mu$	3rd-order total variation diminishing (TVD) Runge–Kutta, high order upwind (convection)	LSM, 2D planar, $\Delta t = 0.05, 0.055$ s, assigned properties
Nichita and Thome (2010) [59]	Pool/flow boiling	Sharp interface model: $S_g = -S_f = \frac{k_{eff} \nabla \alpha_f \nabla T}{h_{fg}}$ BC: $T_{wall} = \text{constant}$ ( $T_{sat} + 8$ K), contact angle = 54°	0.08 × 0.1 m	CLSVOF, 2D/3D planar/ axisymmetric, laminar, water, R134a FLUENT
Kartuzova and Kassemi (2011) [49]	Phase change in pressurized cryogenic storage tank	Sharp interface model: $\dot{m}'' = \frac{k_e \nabla T_s - k_f \nabla T_l}{h_{fg}}$ Schrage model: $\dot{m}'' = \frac{2}{2-\gamma} \left( \frac{M}{2\pi R} \right)^{1/2} \left( \frac{P_g}{\sqrt{T_g}} - \frac{P_l}{\sqrt{T_l}} \right)$ $S_g = -S_f = \dot{m}''  \nabla \alpha $ where $\gamma = 0.01$	PISO, QUICK/compressive (volume fraction), unstructured, $n = 24,215$	VOF, 2D, realizable $k-\epsilon$ , $k-\omega$ SST, $\Delta t = 1 \times 10^{-2} - 10^{-3}$ s, Flow3D, FLUENT
Sun et al. (2012) [42]	Horizontal film boiling	Modified sharp interface model: $S_g = -S_f = \frac{2}{h_{fg}} \frac{k_f \nabla \alpha_f \nabla T}{h_{fg}}$ BC: $T_{wall} = \text{constant}$ ( $T_{sat} + 5$ K)	64 × 128	VOF, 2D, $\Delta t = 1 \times 10^{-2}$ s, assigned properties, FLUENT
Ganapathy et al. (2013) [41]	Flow condensation in rectangular micro-channel	Sharp interface model: $S_g = -S_f = \frac{(k_{eff} \times \nabla T) \cdot \nabla \alpha}{h_{fg}}$ BC: $q''_{wall} = \text{constant}$	CSF (wall adhesion), Geo-reconstruct (volume-fraction), PRESTO (pressure), 1st upwind (momentum), Green Gauss node-based (gradient), quadrilateral, $n = 750,000$ , $D_h = 100 \mu\text{m}$ , $0.1 \times 30$ mm domain, $\Delta c \geq 2 \mu\text{m}$	VOF, 2D planar, laminar, R-134a, HFC-134a Courant = 0.25 (5 max), FLUENT
<i>Schrage model</i> [43] Hardt and Wondra (2008) [46]	Film boiling	Schrage model: $\eta_e = \frac{2\gamma}{2-\gamma} \frac{h_{fg}^2}{\sqrt{2\pi R_{h20}}} \frac{\rho_g}{T_{sat}^{3/2}(P_\infty)}$ where $R_{h20}$ is gas constant for water $j_e^h = \eta_e (T - T_{sat}(P_\infty))$ $Q = \frac{P_g}{V} \int_V  \nabla \alpha  dV$ , $S_g = \frac{Q}{h_{fg}}$ $\gamma = 0.1$ BC: $T_{wall} = \text{constant}$ ( $T_{sat} + 5$ K)	PISO (pressure–velocity coupling), CSF (wall adhesion), Geo-Reconstruct (volume fraction), 1st order implicit (time), 3rd order (convective), central-differencing (diffusive), $64 \times 192/100 \times 300$	VOF, 2D planar, assigned properties, FLUENT
Ranjan et al. (2011) [61]	Film evaporation	Schrage model: $\dot{m}'' = \frac{2\gamma}{2-\gamma} \left( \frac{M}{2\pi R} \right)^{1/2} \left( \frac{P_g}{\sqrt{T_g}} - \frac{P_l}{\sqrt{T_l}} \right)$ BC: $T_w = \text{constant}$	SIMPLE (pressure–velocity coupling), 2nd upwind (convective), 2nd differencing (diffusive), tetrahedral	Octane, water, FLUENT
Doro (2012) [60]	Falling film evaporation	Schrage model: $\eta_e = \frac{2\gamma}{2-\gamma} \frac{h_{fg}^2}{\sqrt{2\pi R_{h20}}} \frac{\rho_g}{T_{sat}^{3/2}(P_\infty)}$ where $R_{h20}$ is gas constant for water $j_e^h = \eta_e (T - T_{sat}(P_\infty))$ $Q = \frac{P_g}{V} \int_V  \nabla \alpha  dV$ , $S_g = \frac{Q}{h_{fg}}$ BC: $q''_{wall} = \text{constant}$	PISO CSF (wall adhesion)	2D, laminar, $\Delta t = 6 \mu\text{s}$ , water, OpenFOAM
Magnini et al. (2013) [47]	Flow evaporation	Modified Schrage by Tanasawa [50]: $\dot{m}'' = \frac{2\gamma}{2-\gamma} \left( \frac{M}{2\pi R} \right)^{1/2} \frac{\rho_g h_{fg} (T - T_{sat}(P_\infty))}{T_{sat}^{3/2}(P_\infty)}$ $S_g = \dot{m}''  \nabla \alpha $ where $\gamma = 1$ BC: $q''_{wall} = \text{constant}$	PISO (pressure–velocity coupling), 1st explicit (VOF), Geo-reconstruct (volume-fraction), Green-Gauss node-based (gradient), 3rd MUSCL (momentum, energy), PRESTO (pressure), $D = 0.5$ mm, $D/\Delta c = 300$	VOF, 2D axisymmetric, laminar, $\Delta t = 5 \times 10^{-7}$ , R113, R134a, R245fa, Courant of 0.25 (5 max), FLUENT
<i>Lee model</i> [51] Wu et al. (2007) [52]	Flow boiling in serpentine tube	Lee model: $S = r_i \alpha_f \rho_f \frac{(T - T_{sat})}{T_{sat}}$ for $T > T_{sat}$ $S = r_i \alpha_g \rho_g \frac{(T - T_{sat})}{T_{sat}}$ for $T < T_{sat}$ $r_i = 0.1 \text{ s}^{-1}$ BC: $q''_{wall} = \text{constant}$	SIMPLE (pressure–velocity coupling)	$\Delta t = 1 \times 10^{-5}$ , R141B, FLUENT
Yang et al. (2008) [55]	Flow boiling in a coiled tube	Lee model: $S = r_i \alpha_f \rho_f \frac{(T - T_{sat})}{T_{sat}}$ for $T > T_{sat}$ $S = r_i \alpha_g \rho_g \frac{(T - T_{sat})}{T_{sat}}$ for $T < T_{sat}$ $r_i = 100 \text{ s}^{-1}$ BC: $q''_{wall} = \text{constant}$	PISO (pressure–velocity coupling), CSF (wall adhesion), 2nd upwind (momentum), 2nd upwind (energy), hexahedral, $n = 118,800$ ( $135 \times 880$ ), $D = 6$ mm	VOF, realizable $k-\epsilon$ , $\Delta T_{sat} \leq 1$ K, R141B, FLUENT
De Schepper et al. (2009) [53]	Flow boiling	Lee model: $S = r_i \alpha_f \rho_f \frac{(T - T_{sat})}{T_{sat}}$ for $T > T_{sat}$ $S = r_i \alpha_g \rho_g \frac{(T - T_{sat})}{T_{sat}}$ for $T < T_{sat}$ $r_i = 0.1 \text{ s}^{-1}$ BC: $q''_{wall} = \text{constant}$	PISO (Pressure–velocity coupling), Geo-Reconstruct (volume fraction), 2nd upwind (momentum, energy), hexahedral, $n = 1,993,648$ , $D = 0.0525$ m, $L = 11.3$ m	VOF, 3D, $\Delta t = 0.001$ s, standard $k-\epsilon$ model, gas-oil, FLUENT

Table 1 (continued)

Author(s)	System	Model	Discretization scheme & mesh	Remarks
Fang et al. (2010) [56]	Flow boiling in micro-channel	Lee model: $S = r_i \alpha_f \rho_f \frac{(T - T_{sat})}{T_{sat}}$ for $T > T_{sat}$ $S = r_i \alpha_g \rho_g \frac{(T - T_{sat})}{T_{sat}}$ for $T < T_{sat}$ , $r_i = 100 \text{ s}^{-1}$ BC: $q''_{wall} = \text{constant}$ , contact angle = $140^\circ$	PISO (pressure-velocity coupling) Geo-Reconstruct (volume fraction), algebraic multigrid (AMG), structured orthogonal, $n = 191,400$ , $330 \times 20 \times 25$ (channel)/ $0.3 \times 0.15 \times 5 \text{ mm}$ channel	VOF, 3D, laminar, FLUENT
Alizadeh-dakhel et al. (2010) [54]	Thermosyphon	Lee model: $S = r_i \alpha_f \rho_f \frac{(T - T_{sat})}{T_{sat}}$ for $T > T_{sat}$ $S = r_i \alpha_g \rho_g \frac{(T - T_{sat})}{T_{sat}}$ for $T < T_{sat}$ , $r_i = 0.1 \text{ s}^{-1}$ BC: $q''_{wall} = \text{constant}$	SIMPLE (pressure-velocity coupling), 1st upwind (momentum, energy), Geo-Reconstruct (volume fraction), $n = 47,124$ , finer mesh near walls	VOF, 2D, laminar, $\Delta t = 0.001 \text{ s}$ , FLUENT
Da Riva and Del Col (2011) [57]	Flow condensation in a circular tube	Lee model: $S = r_i \alpha_f \rho_f \frac{(T - T_{sat})}{T_{sat}}$ for $T > T_{sat}$ $S = r_i \alpha_g \rho_g \frac{(T - T_{sat})}{T_{sat}}$ for $T < T_{sat}$ , $r_i = 7.5 \times 10^5 - 1 \times 10^7 \text{ s}^{-1}$ BC: $T_{wall} = \text{constant}$	Modified High Resolution Interface Capturing (HRIC) (volume fraction), hexahedral, $n = 1,150,000$ for 3D, square, $n = 25,000$ for 2D, $D = 1 \text{ mm}$	VOF, 2D axisymmetric and 3D, CSF, $k-\omega$ SST ( $Pr_T = 0.85$ ), R134a, FLUENT
Chen et al. (2014) [58]	Flow condensation in rectangular micro-channel	Lee model: $S = r_i \alpha_f \rho_f \frac{(T - T_{sat})}{T_{sat}}$ for $T > T_{sat}$ $S = r_i \alpha_g \rho_g \frac{(T - T_{sat})}{T_{sat}}$ for $T < T_{sat}$ , $r_i = 100 \text{ s}^{-1} \text{ K}^{-1}$ BC: $q''_{wall} = \text{constant}$	Hexahedral, $n = 200,000$ , $D_h = 100 \mu\text{m}$ , $1 \times 300 \text{ mm}$ domain	VOF, 3D, realizable $k-\epsilon$ , $\Delta t = 1 \times 10^{-6}$ , $\Delta T_{sat} \leq 0.1^\circ\text{C}$ , FLUENT
Present study	Downflow condensation in a circular tube	Lee model: $S = r_i \alpha_f \rho_f \frac{(T - T_{sat})}{T_{sat}}$ for $T > T_{sat}$ $S = r_i \alpha_g \rho_g \frac{(T - T_{sat})}{T_{sat}}$ for $T < T_{sat}$ , $r_i = 10,000 \text{ s}^{-1}$ BC: $q''_{wall}$ from experimental data	PISO (pressure-velocity coupling), CSF (wall adhesion), Least Squares Cell Based (gradient), Body Force Weighted (pressure), 3rd-order MUSCL (momentum), Geo-Reconstruct (volume fraction), 1st Order Upwind (turbulent kinetic energy, specific dissipation rate), 2nd order upwind (energy), 1st Order Implicit (transient formulation), quadrilateral, $n = 3,734,919$ , finer mesh near wall, $\Delta x = 1.3 \mu\text{m}$ min., $D = 11.89 \text{ mm}$ , $\phi = 11.89 \times 807 \text{ mm}$	VOF, 2D axisymmetric, $k-\omega$ SST ( $Pr_T = 0.85$ ), FC-72, Courant = 2 max., variable $\Delta t > 1 \times 10^{-8} \text{ s}$ , $\Delta T_{sat} \leq 2^\circ\text{C}$ , FLUENT

numerical convergence problems. However, in their simulation of micro-channel condensation in microgravity, Da Riva and Del Col [57] used very large values of  $r_i = 7.5 \times 10^5 \text{ s}^{-1}$  for a low mass velocity of  $G = 100 \text{ kg/m}^2 \text{ s}$ , and  $r_i = 1.0 \times 10^7 \text{ s}^{-1}$  for a high mass velocity of  $G = 800 \text{ kg/m}^2 \text{ s}$ . Chen et al. [58] used the following modified Lee model,

$$S_g = -S_f = r_{i,Chen} \alpha_g \rho_g (T - T_{sat}) \quad \text{for condensation } (T < T_{sat}), \quad (9a)$$

and

$$S_g = -S_f = r_{i,Chen} \alpha_f \rho_f (T - T_{sat}) \quad \text{for evaporation } (T > T_{sat}), \quad (9b)$$

where  $r_{i,Chen}$  was set to  $100 \text{ s}^{-1} \text{ K}^{-1}$ . Notice that the units of  $r_{i,Chen}$  are different from those of  $r_i (\text{s}^{-1})$  because of deletion of the temperature denominators from the original Eqs. (9a) and (9b). Therefore, the corresponding  $r_i$  at  $T_{sat} = 60^\circ\text{C}$  (saturation temperature for the FC-72 working fluid used in their study) is equivalent to using the original Lee model with  $r_i = 33,315$ .

Table 1 provides a comprehensive summary of literature concerning the implementation of different computational phase change models.

#### 1.4. Objectives of study

The present study includes both experimental and computational investigations of condensation of FC-72 in vertical downflow in a circular tube. A highly instrumented condensation test module is used to map detailed axial variations of both the wall heat flux and wall temperature, which are also used to determine the axial variation of the condensation heat transfer coefficient. The experimentally determined parameters are compared to predictions of a two-dimensional and axisymmetric computational model using FLUENT. This paper will provide detailed information on the choice of interfacial phase change model, numerical methods used, and convergence criteria.

## 2. Experimental methods

The computational results are evaluated against experimental data obtained using a condensation facility utilizing a tube-in-tube condensing module, which employs FC-72 as working fluid. Fig. 1(a) shows a schematic of the condensation facility, which is comprised of a primary loop for the FC-72 and two secondary water cooling loops. Condensation is achieved by transferring heat from the primary loop to the first water loop via the condensation module. Using a gear pump, FC-72 liquid is passed through one of several rotameters connected in parallel for flow rate measurement, followed by a 14.2 kW pre-heater, where the FC-72 is converted to vapor. The slightly superheated FC-72 vapor then enters the condensation module where is gradually converted to liquid by rejecting heat to a counter-flow of water from the first secondary water loop. Exiting the condensation module, the FC-72 passes through a plate-type condenser, where it is cooled by the second water cooling loop, followed by an air-cooled condenser to bring any vapor exiting the test module to subcooled liquid state before returning to the primary loop's reservoir.

Two separate systems are used to rid the FC-72 from any dissolved non-condensable gases prior to performing any tests. The first is a vacuum pump that is used initially to remove any non-condensables by creating vacuum inside the system. The second is an air-cooled condenser. To assist the deaeration process, the reservoir of the primary loop is fitted with two immersion heaters to produce vigorous boiling in the FC-72 liquid. A mixture of vapor and non-condensable gases is passed through the deaeration



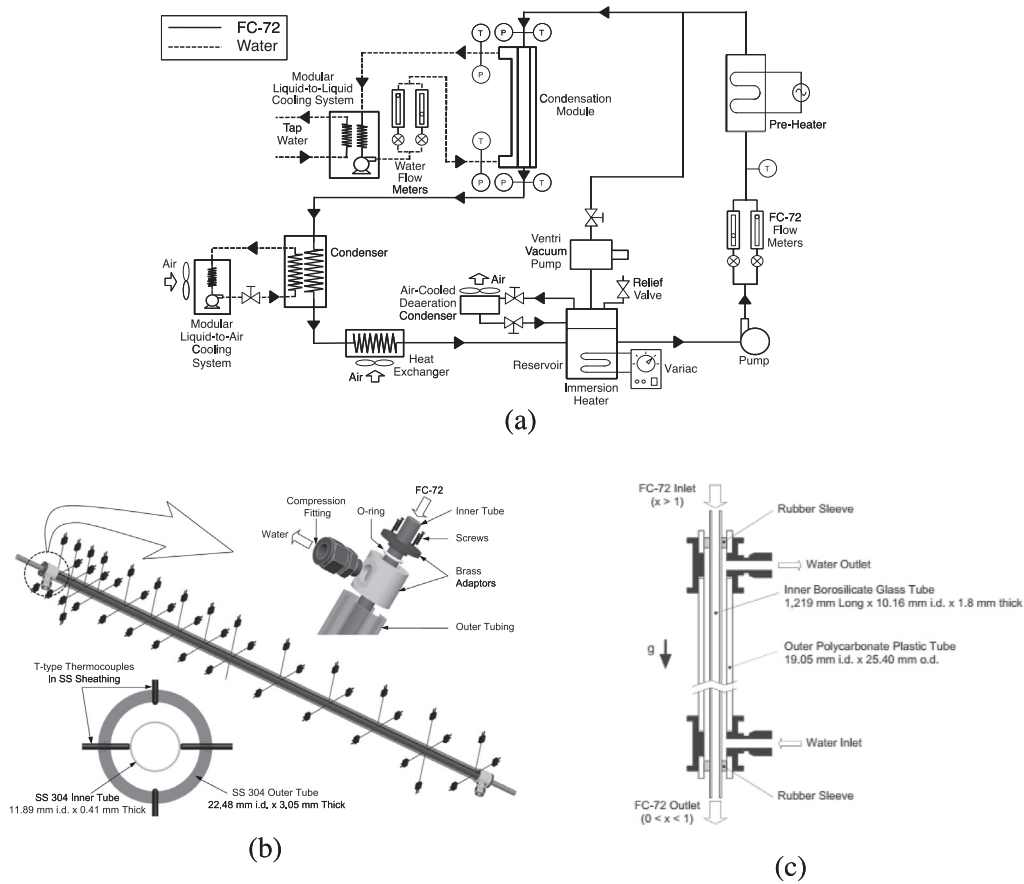


Fig. 1. Schematics of (a) flow delivery system, (b) heat transfer module, and (c) flow visualization module.

condenser, where most of the vapor is recaptured by condensation as the non-condensable gases are purged to the ambient.

Two separate modules are used in this facility. The first is used in the present study to obtain detailed heat transfer data, and the other for flow visualization; both feature tube-in-tube construction. For the heat transfer module, Fig. 1(b), the FC-72 flows through the inner 11.89-mm i.d. stainless steel tube and is cooled by a counter-flow of water through the annulus. The total condensation length of this module is 1259.84 mm. Type-T thermocouples are located at the outer surface of the inner tube at 14 axial locations to measure the outer wall temperature, with two diametrically-opposite thermocouples installed at each axial location to ensure vertical and symmetrical alignment of the condensation module. The water temperature is also measured at the same 14 axial locations, with three additional water thermocouples installed at each of three axial locations near the inlet, middle and exit to check for any circumferential asymmetry. Both temperature and pressure are also measured in the FC-72 and water inlets and outlets. Fig. 1(c) illustrates the construction of the second, flow visualization module.

Further details concerning the construction and instrumentation of the fluid delivery system, measurement methods and

measurement accuracies are provided in [25]. The operating conditions of the experimental study are given in Table 2.

### 3. Computational methods

#### 3.1. Governing equations

The VOF method [32] adopted in FLUENT is used to compute the conservation equations for liquid and vapor while also accounting for mass transfer between the two phases. The continuity equations are expressed as [62]

$$\frac{\partial}{\partial t}(\alpha_f \rho_f) + \nabla \cdot (\alpha_f \rho_f \vec{u}_f) = S_f, \quad (10a)$$

vapor phase:

$$\frac{\partial}{\partial t}(\alpha_g \rho_g) + \nabla \cdot (\alpha_g \rho_g \vec{u}_g) = S_g. \quad (10b)$$

The momentum and energy equations, which are written for the combined phases, are expressed, respectively, as [62]

Table 2  
Operating conditions of the experimental study.

	$G$ [kg/m <sup>2</sup> s]	$P_{in}$ [kPa]	$\Delta P$ [kPa]	$T_{in}$ [°C]	$x_{e,in}$	$G_w$ [kg/m <sup>2</sup> s]	$T_{w,in}$ [°C]	$T_{w,out}$ [°C]	$\bar{q}''_{wall}$ [W/cm <sup>2</sup> ]	$\bar{h}$ [W/m <sup>2</sup> K]
Max.	459.0	209.9	13.7	86.6	1.08	308.2	29.7	45.1	9.02	2715.02
Min.	184.4	108.6	1.0	63.5	1.04	37.0	22.3	29.9	2.11	1359.75

momentum:

$$\frac{\partial}{\partial t}(\rho \vec{u}) + \nabla \cdot (\rho \vec{u} \vec{u}) = -\nabla P + \nabla \cdot [\mu(\nabla \vec{u} + \nabla \vec{u}^T)] + \rho \vec{g} + \vec{F}, \quad (11)$$

energy:

$$\frac{\partial}{\partial t}(\rho E) + \nabla \cdot (\vec{u}(\rho E + P)) = \nabla \cdot (k_{eff} \nabla T) + Q, \quad (12)$$

where  $E$  [J/kg] is the energy per unit mass, which is determined from [62]

$$E = \frac{\alpha_f \rho_f E_f + \alpha_g \rho_g E_g}{\alpha_f \rho_f + \alpha_g \rho_g}, \quad (13)$$

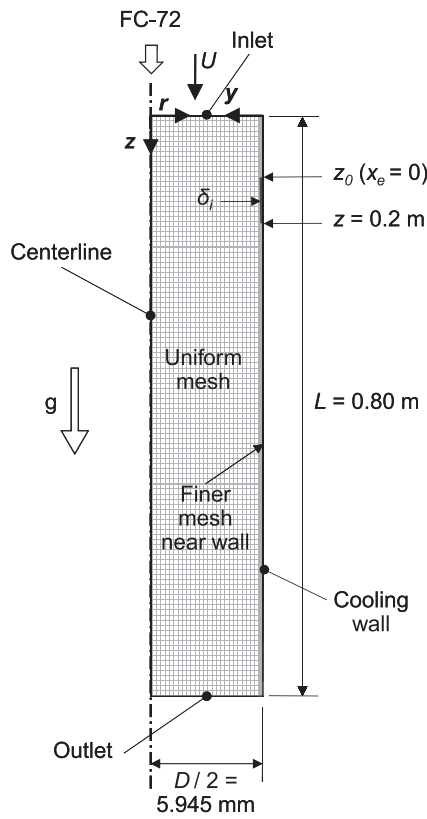


Fig. 2. Computational domain.

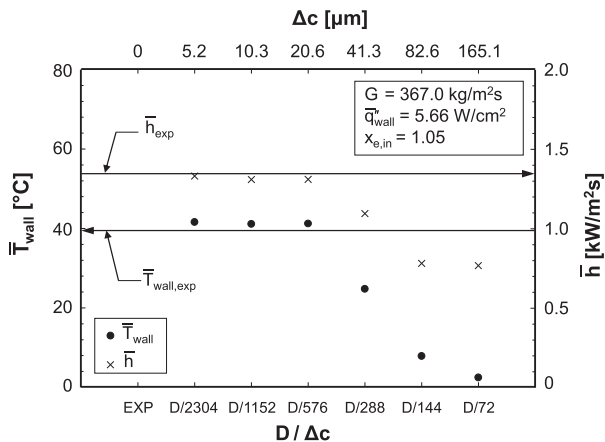


Fig. 3. Averaged wall temperature and condensation heat transfer coefficient for different mesh sizes.

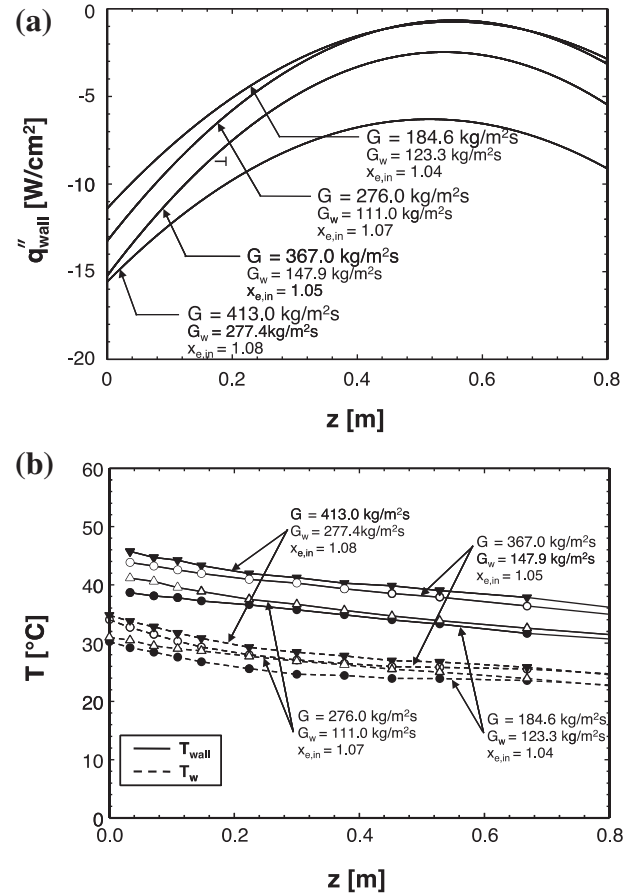


Fig. 4. Experimentally determined axial variations of (a) wall heat flux and (b) water and outer wall temperatures for four operating conditions.

Table 3  
Solution methods and controls.

Discretization method	
Pressure-velocity coupling	Pressure-implicit with splitting of operators (PISO)
	Skewness correction = 1
	Neighbor correction = 1
Gradient	Least squares cell based
Pressure	Body force weighted
Momentum	Third-order monotonic upstream-centered scheme for conservation laws (MUSCL)
Volume fraction	Geo-reconstruct
Turbulent kinetic energy	First order upwind
Specific dissipation rate	First order upwind
Energy	Second order upwind
Transient formulation	First order implicit
Under-relaxation factors	
Pressure	0.3
Density	1
Body forces	
Vaporization mass	
Turbulent viscosity	
Energy	
Momentum	0.7
Turbulent kinetic energy	0.8
Specific dissipation rate	

**Table 4**

Thermophysical properties used in the computational study.

	$T_{sat}$ [°C]	$h_{fg}$ [J/kg]	$\rho_g$ [kg/m <sup>3</sup> ]	$c_{p,g}$ [J/kg K]	$k_g$ [W/m K]	$\mu_g$ [N s/m <sup>2</sup> ]	$\rho_f$ [kg/m <sup>3</sup> ]	$c_{p,f}$ [J/kg K]	$k_f$ [W/m K]	$\mu_f$ [N s/m <sup>2</sup> ]	$\sigma$ [N/m]
Max.	75.0	82,721	23.1	1259.8	0.015	$1.22 \times 10^{-5}$	1593.5	1130.5	0.054	$4.24 \times 10^{-4}$	$8.2 \times 10^{-3}$
Min.	58.4	77,623	14.2	1212.0	0.014	$1.16 \times 10^{-3}$	1530.5	1104.8	0.052	$3.60 \times 10^{-4}$	$6.5 \times 10^{-3}$

$$\rho = \alpha_f \rho_f + \alpha_g \rho_g, \quad (14a)$$

$$\mu = \alpha_f \mu_f + \alpha_g \mu_g, \quad (14b)$$

and

$$k_{eff} = \alpha_f k_f + \alpha_g k_g. \quad (14c)$$

In the present computations, mass transfer due to condensation is accounted for by using the appropriate mass source terms,  $S_f$  and  $S_g$ , and the corresponding energy transfer term is accounted for as  $Q = h_{fg} S_f$ .

### 3.2. Computational domain

Fig. 2 shows the computation domain used in the present study. This domain is two-dimensional and axisymmetric, simulating vertical downflow condensation in a circular tube, and uses actual dimensions of the experimental condensation module. The length of the domain is set longer than the actual length of 0.80 m to avoid any end effect at the lower outlet. A quadrilateral mesh is adopted for the entire domain. The mesh is uniform everywhere

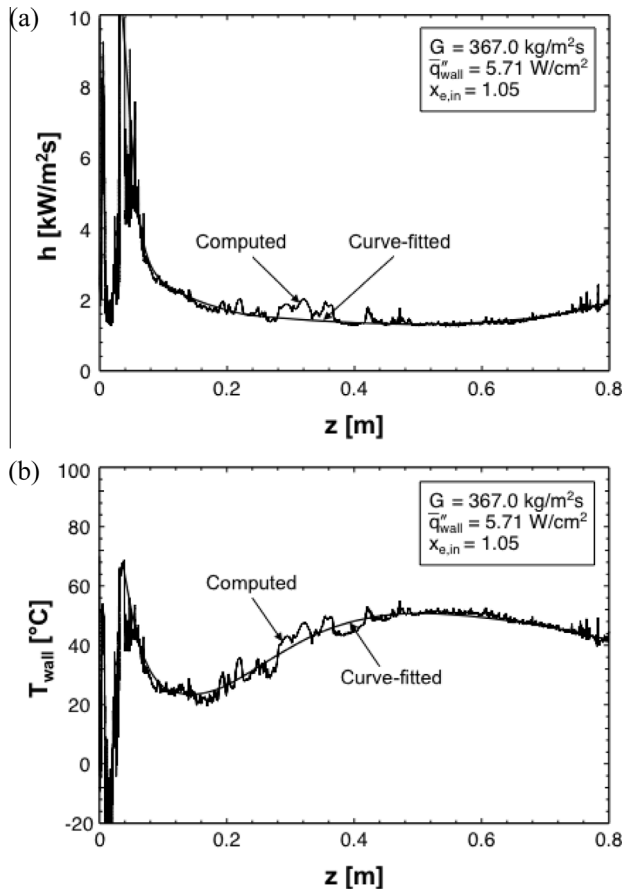


**Fig. 5.** Computed and spline curve-fitted axial variations of (a) condensation heat transfer coefficient and (b) wall temperature using  $r_i = 10,000$ .

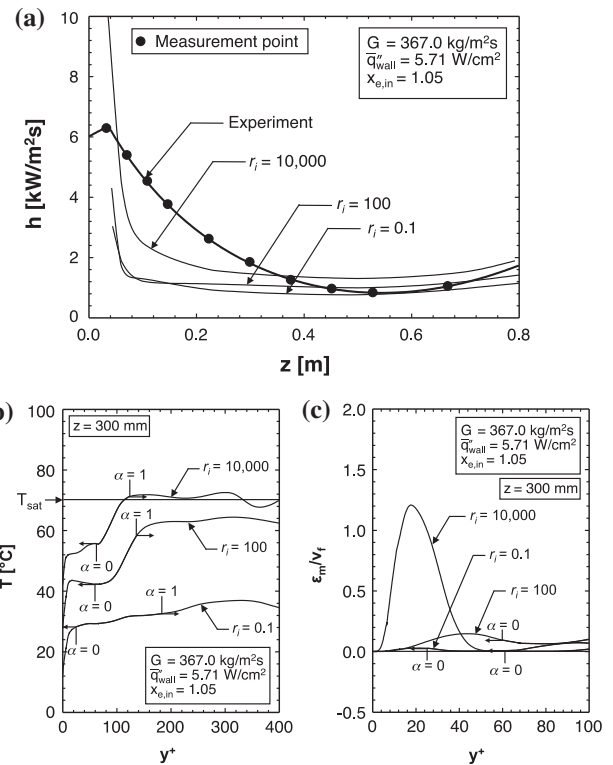


**Fig. 6.** (a) Axial variations of experimental and computed local condensation heat transfer coefficients, and variations of (b) temperature with  $y^*$  and (c) eddy diffusivity with  $y^*$  for  $r_i$  of 0.1, 100 and 10,000.

except near the condensation wall, where it is gradually refined to capture thin liquid film formation in the upstream region as well as stronger gradients across the liquid film. Grid independence is verified by averaging the computed condensation heat transfer coefficient and wall temperature over the length  $0.2 < z < 0.8$  m for each of six different grid sizes, and comparing the average values with experimental results. The region  $z < 0.2$  m is intentionally excluded for the averaging because of difficulty modeling this upstream region as discussed later. Fig. 3 shows the average heat transfer coefficient and wall temperature reach asymptotic values just below a cell (mesh) size of  $\Delta c < 20.6 \mu\text{m}$ ;  $\Delta c = 10.3 \mu\text{m}$  is therefore adopted in all the present computations. However, the minimum cell size of  $\Delta c = 1.3 \mu\text{m}$  is used near the condensing wall, which ensures more than five cells are within  $y^* < 5$ .

### 3.3. Initialization and boundary conditions

Like the actual experiments, FC-72 is assumed to be introduced into the channel in slightly superheated vapor state (4–7 °C superheat) and constant inlet velocity of  $U = G/\rho_g$ , matching actual inlet operating conditions tested experimentally.

Turbulence intensity,  $I$ , for each case is estimated from the following empirical relation for pipe flows [62],

$$I = \frac{u''}{u} = 0.16 Re_D^{-1/8}. \quad (16)$$



The axial variation of the wall heat flux is obtained from the experimental data and employed as boundary condition using FLUENT's user defined function DEFINED\_PROFILE. The heat flux is determined from the local differential sensible heat rise of the cooling water according to

$$q''_{wall} = \dot{m}_w c_{p,w} (T_{w,i+1} - T_{w,i}) / (\pi D). \quad (17)$$

Fig. 4 shows axial variations of the experimentally determined wall heat flux for four FC-72 mass velocities that are examined in the computational study.

For the cooling wall, default values of 0 m, 0.5 and 90° are used for roughness height, roughness constant and contact angle, respectively, due to relative insensitivity of the condensation heat transfer coefficient to the values of these parameters after the film is established.

One of the main challenges in the computational model is the difficulty initiating a continuous liquid film in the upstream region of the condensation tube. While an actual liquid film is observed in the experiments near the inlet, the computational model could not generate a continuous film in the same region, but farther downstream. In other words, the phase change relations used in the computational model could not accurately replicate the actual physical phenomena. Instead, the model is found to generate a certain mass of liquid in random discrete cells at the wall once it detects temperatures below  $T_{sat}$ , rather than generate a continuous film. Using a very large value for the mass transfer intensity factor,  $r_i$ , was supposed to remove this discrepancy. Instead, it further destabilized the numerical solution. Hence, a different numerical approach is adopted to assist the solution process. A very thin liquid film of uniform thickness  $\delta_i$  is artificially applied from  $z = z_0$ , where  $x_e = 1$ , to  $z = 0.2$  m, to numerically initiate the upstream formation of the liquid film and also significantly reduce convergence

time. An appropriate value for  $\delta_i$ , which is determined from a recent annular flow condensation model [63], is applied from  $z = z_0$  to  $z = 0.2$  m. The location  $z_0$  corresponding to  $x_e = 1$  is obtained from the simple energy balance

$$x_e = 1 + c_{p,g} (T_{in} - T_{sat}) / h_{fg}, \quad (18)$$

where  $T_{in}$  is the temperature of the superheated vapor at the tube inlet. Depending on operating conditions, the applied initial liquid film thickness varies from  $\delta_i = 49\text{--}77$   $\mu\text{m}$ , less than 0.6% of the channel diameter. Using the appropriate  $\delta_i$  value, the computational model predicts downstream film thicknesses much greater than  $\delta_i$ . The use of an artificial film upstream with thickness  $\delta_i$  is also very instrumental in achieving acceptable results using a reasonable value for  $r_i$ , rather than the very high values adopted by Da Riva and Del Col [57].

### 3.4. Solution technique

Downflow condensation in the circular tube is simulated with ANSYS FLUENT using a pressure-based solver. Explicit scheme of the VOF model is used in Multiphase Model of FLUENT with default values for volume fraction cutoff and Courant number of  $1 \times 10^{-6}$  and 0.25, respectively. Turbulence effects are taken into account using the Shear-Stress Transport (SST)  $k\text{--}\omega$  model [64] with a turbulent damping factor of 10. Realizable  $k\text{--}\epsilon$  model [65] is another popular turbulent model that has been used to tackle both adiabatic and diabatic turbulent single-phase and two-phase flows [49,55,58,66,67]. However, it is avoided in the present study because of its tendency to create appreciable disturbances at the interface for relatively low  $r_i$  values when the interfacial temperature is still much lower than  $T_{sat}$ . In the present computations, the Continuum Surface Force (CSF) model [68] with wall adhesion

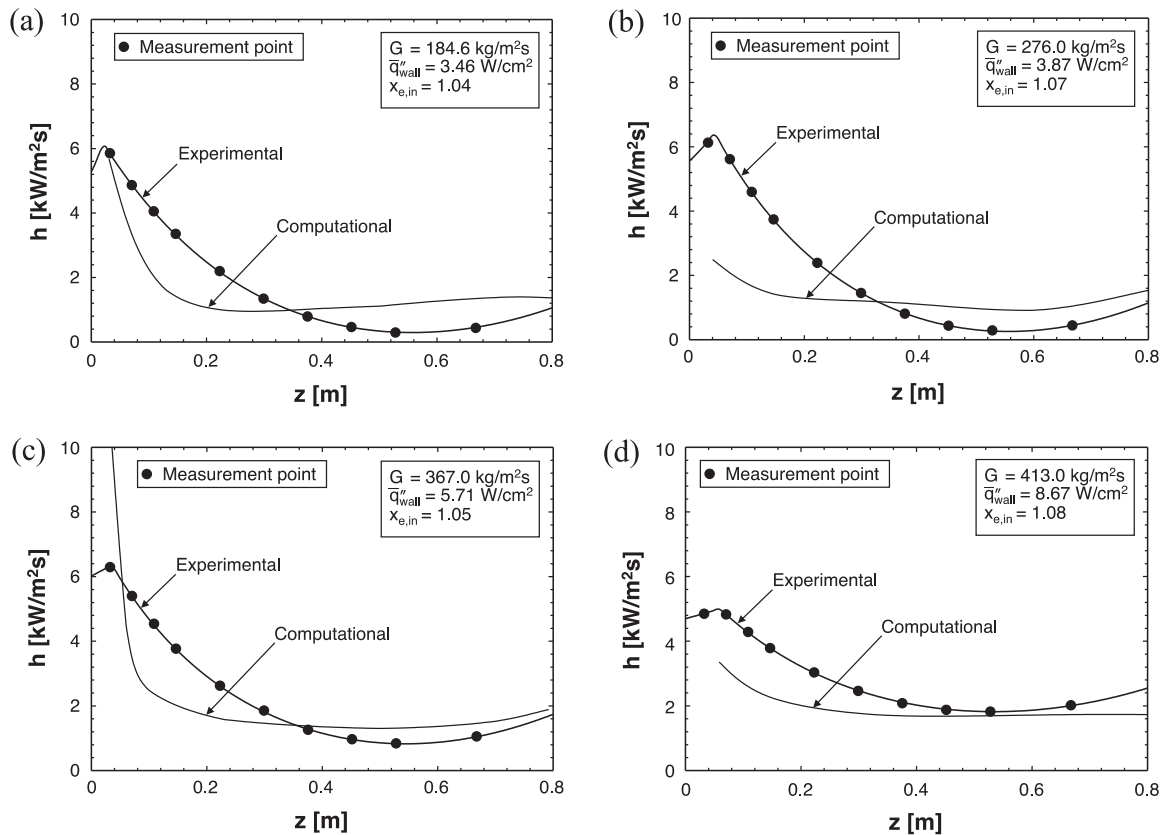


Fig. 7. Axial variations of experimental and computed local condensation heat transfer coefficients for four operating conditions.

is used to tackle surface tension force. The pressure-implicit with splitting of operators (PISO) scheme [69], with the skewness and neighbor corrections of unity, is used to tackle pressure–velocity coupling. Least-Squares Cell-Based formulation is used for gradient discretization. Magnini et al. [47] reported that Green-Gauss Node-Based formulation is the best option for gradient discretization, however, this formulation was found to pose convergence problems when used in initial attempts in conjunction with realizable  $k$ - $\varepsilon$  model, which is why the Green-Gauss Node-Based formulation was avoided altogether. The Body Force Weighted scheme, which is recommended for situation involving large body force, and **third-order Monotonic Upstream-centered Scheme** for Conservation Laws (MUSCL) [70], are used for pressure and momentum discretization, respectively. **PREssure STaggering Option (PRESTO)** and Quadratic Upstream Interpolation for Convective Kinematics (QUICK) [71] schemes were initially tested for the pressure and momentum discretization, respectively, but abandoned after showing minute differences in predictions, excepting a minor increase in the condensation heat transfer coefficient. Piecewise Linear Interface Calculation (PLIC) algorithm (named Geo-Reconstruct in FLUENT) [72] is used for volume fraction discretization, first-order upwind scheme [73] for both turbulent kinetic energy and specific dissipation rate, and second-order upwind scheme [73] for energy discretization. Complete details of the solution methods and thermophysical properties used in this study are provided in Tables 3 and 4, respectively.

## 4. Results

### 4.1. Determination of optimum mass transfer intensity factor, $r_i$

Determining an appropriate value for the mass transfer intensity factor,  $r_i$ , is one of the most important tasks when using the Lee

model [51] for phase change applications since this value will affect, not only the computed temperatures, but the detailed features of the entire two-phase flow field as well. Therefore, different values for  $r_i$  are examined in pursuit of good agreement between computed and measured temperatures and condensation heat transfer coefficients. Before addressing the optimum value for  $r_i$ , it is important to note that the computed heat transfer coefficient and temperature displayed oscillations and fluctuations, especially in the inlet region. These features are the result of interfacial waves, vapor bubble entrainment in the annular liquid film, and liquid droplet entrainment in the vapor core. To better represent computed trends and their comparisons with the experimental data, the computed axial variations of heat transfer coefficient,  $h$ , and temperature,  $T$ , are spline curve-fit using MATLAB Curve Fitting Toolbox [74], as depicted in Fig. 5(a) and (b), respectively.

Fig. 6(a)–(c) compare axial variations of  $h$ , temperature profiles and eddy momentum diffusivity profiles, respectively, computed using three different values of  $r_i = 0.1, 100$  and  $10,000$ . Also included in Fig. 6(a) is the axial variation of the experimentally determined  $h$ . The temperature and eddy diffusivity profiles are plotted versus dimensionless distance from the wall,  $y^+$ , which is defined as

$$y^+ = \frac{yu^*}{\nu_f} = \frac{y}{\nu_f} \sqrt{\frac{\tau_{wall}}{\rho_f}}. \quad (19)$$

Notice how different  $r_i$  values lead to different predictions of the condensation heat transfer coefficient, temperature and eddy momentum diffusivity. These differences are rooted in the fact that  $r_i$  is not only a relaxation factor, but also determines mass transfer rate, which affects both  $T_{wall}$  and liquid film thickness. For condensation, vapor temperature begins to decrease near the wall in response to heat removal at the wall. Once the vapor temperature falls below  $T_{sat}$ , positive values of the volumetric mass source term

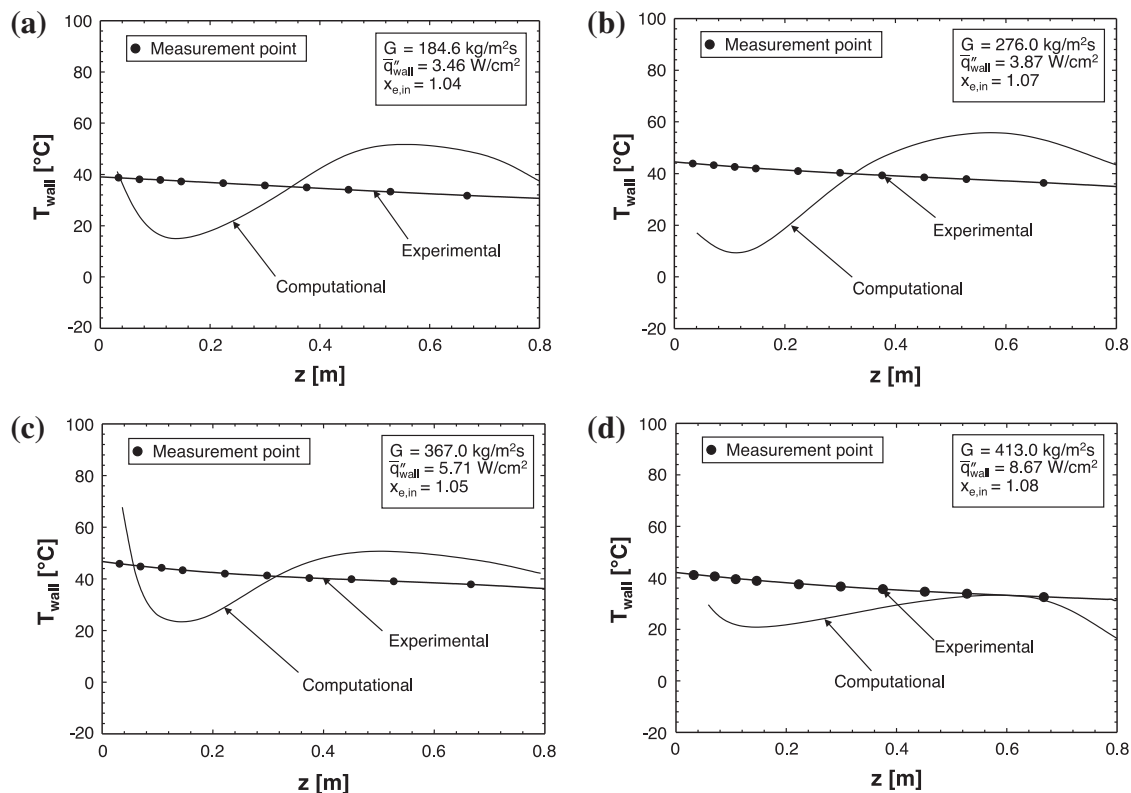


Fig. 8. Axial variations of experimental and computed wall temperatures for four operating conditions.

for liquid,  $S_f$ , and energy source term due to phase change,  $Q$ , respectively, are realized in accordance with Eqs. (8a) and (15), respectively. This causes heat removal at the wall to be compensated in part by phase change from vapor to liquid, rather than by reduction of vapor temperature alone. It is observed that the use of a low value of  $r_i = 0.1$  results in a relatively small  $Q$  that is insufficient to resist the decrease in the interface and wall temperatures. Notice in Fig. 6(b) how  $r_i = 0.1$  causes appreciable deviation of interfacial temperature,  $T_i$ , from  $T_{sat}$ . This also leads to lower predictions of  $h$  compared to experimental values as depicted in Fig. 6(a) since  $h = q''_{wall}/(T_{sat} - T_{wall})$ . As  $r_i$  is increased to 100, both  $S_f$  and  $Q$  become large enough to compensate for heat removal at the wall, which causes  $T_i$  to approach  $T_{sat}$ , Fig. 6(b), and better predictions of  $h$ ,

Fig. 6(a). Increasing  $r_i$  further to 10,000 shows even better agreement between  $T_i$  and  $T_{sat}$ , Fig. 6(b), and computed and experimental  $h$ , Fig. 6(a). However, much higher values of  $r_i$  yielded severe oscillations in the computed interface and, as suggested in Refs. [55–57], caused the solution to diverge.

Fig. 6(c) shows the magnitude of peak eddy diffusivity in the liquid film is very sensitive to  $r_i$ . This dependence is attributed in part to liquid film thickness changes relative to the value of  $r_i$  used. Mascarenhas and Mudawar [66] found computed eddy diffusivity in free-falling liquid films that are subjected to sensible heating to fluctuate between the wave crests and troughs. Since a low  $r_i$  delays phase change from vapor to liquid at the interface, the location of  $\alpha = 0$  in the present study, where eddy diffusivity goes to

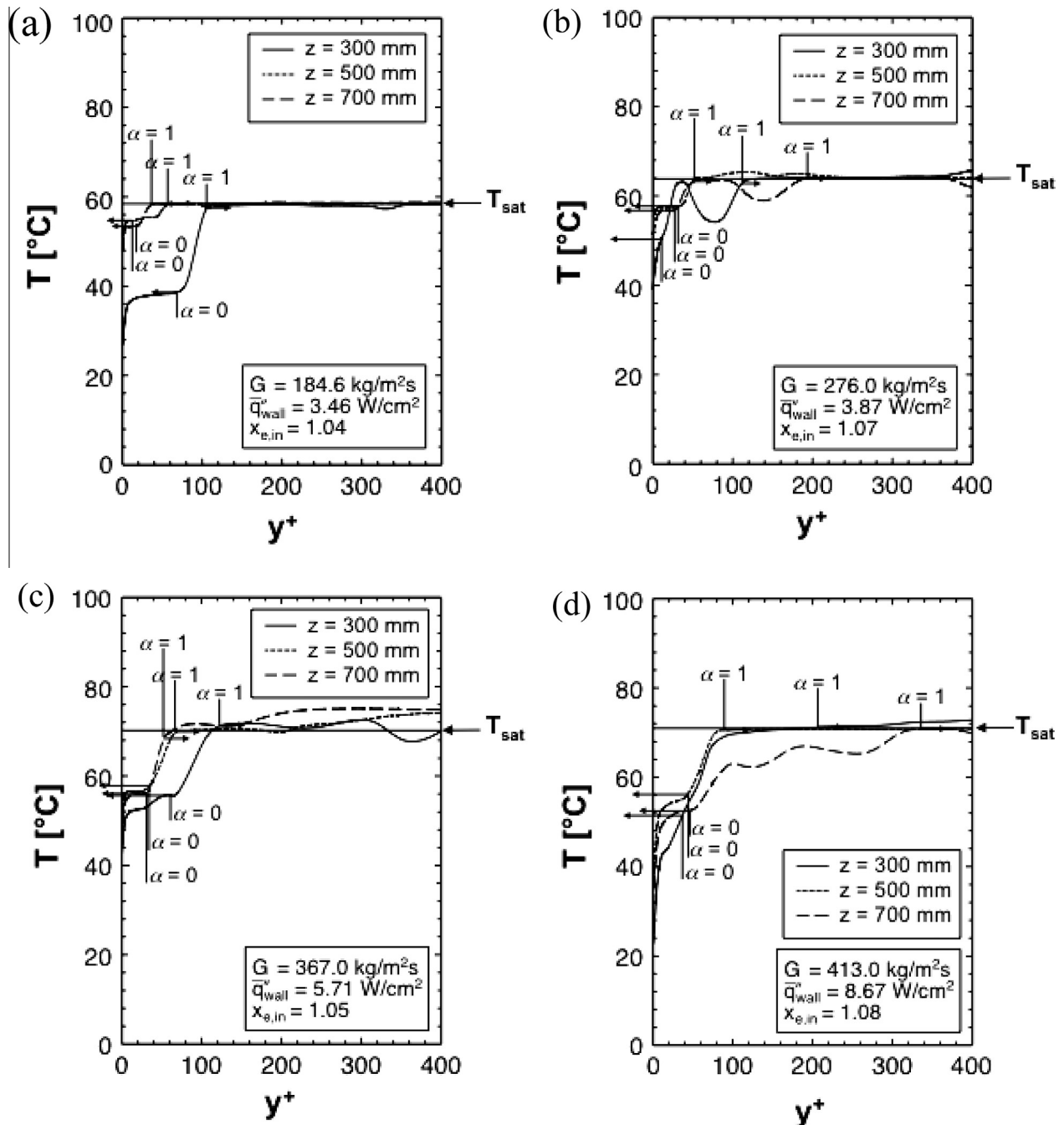


Fig. 9. Variation of computed temperature with dimensionless distance from the wall at three axial locations for four operating conditions.

zero, moves closer to the wall, causing the magnitude of peak eddy diffusivity to decrease. Da Riva and Del Col [57] obtained thinner liquid films with sharper interface when using very large  $r_i$  values in their study of horizontal condensation along a mini-channel. However, increasing  $r_i$  in the present study did not change the average liquid film thickness, which may be due to stronger gravitational effects in vertical downflow compared to horizontal flow.

One important finding from the computed eddy momentum diffusivity profiles in Fig. 6(c) is the dampening of eddy diffusivity near the interface for all three values of  $r_i$ . This important behavior will be explained later.

Based mostly on the  $h$  and  $T$  trends with  $r_i$  in Fig. 6(a) and (b), respectively, the value of  $r_i = 10,000$  is used to generate all computational results presented hereafter.

#### 4.2. Heat transfer results

Fig. 7(a)–(d) compare experimental and computed variations of  $h$  along the tube for four FC-72 mass velocities of  $G = 184.6, 276.0, 367.0$  and  $413.0 \text{ kg/m}^2 \text{ s}$ , respectively. Overall, there is good agreement in the middle and downstream regions of the channel for all four FC-72 mass velocities. But, while both predicted and experimental values show the expected large values in the inlet region where the film begins to form, there are appreciable deviations in the same region. Similar inlet region discrepancies were observed in comparisons between analytical model predictions and experimental data for condensation in tubes [25,26,63], and this may be attributed in part to the difficulty obtaining accurate data in this region because of strong axial conduction effects in the metallic condensation tube.

Notice that, unlike the trends in Fig. 7(a)–(c) for the three lowest  $G$  values, the computed  $h$  values for the highest  $G$ , Fig. 7(d), uniformly underpredicts experiment. This points to the merits of using a value even higher than  $r_i = 10,000$  for the highest  $G$ . However, using increasing values of  $r_i$  with increasing  $G$  compromises consistency in the utilization of a computational model.

Fig. 8(a)–(d) compare experimental and computed variations of  $T_{\text{wall}}$  along the tube for  $G = 184.6, 276.0, 367.0$  and  $413.0 \text{ kg/m}^2 \text{ s}$ , respectively. While the experimental  $T_{\text{wall}}$  shows a fairly linear drop, the computed  $T_{\text{wall}}$  shows lower values upstream and higher downstream, but with an average approaching the measured. Like Fig. 7(d), only the highest  $G$  shows predictions uniformly underpredicting the measured.

Fig. 9(a)–(d) show computed temperature profiles for  $G = 184.6, 276.0, 367.0$  and  $413.0 \text{ kg/m}^2 \text{ s}$ , respectively. These plots show interfacial temperatures are predicted within  $\pm 2^\circ \text{C}$  of  $T_{\text{sat}}$ . The liquid film is shown getting thicker towards to the exit, especially for  $G = 276.0$  and  $413.0 \text{ kg/m}^2 \text{ s}$ .

As shown earlier in Fig. 6(c), eddy momentum diffusivity is dampened near the interface. This important phenomenon is believed to be the result of suppression of turbulent fluctuations at the interface by surface tension forces. As discussed in Ref. [75], similar interfacial dampening has been reported in several previous studies on free-falling films, as well as in the recent computational study by Mascarenhas and Mudawar [66,67] concerning free-falling films subjected to sensible heating. As shown in Fig. 6(b) as well as Fig. 9(a)–(d), the liquid film temperature exhibits an unusual profile with a mild gradient in the middle of the film and large gradients both at the wall and interface. This behavior is explained with the aid of Fig. 10(a) and (b). An eddy diffusivity profile is shown having zero value both at the wall and the interface, and a maximum somewhere in between. The temperature profile in Fig. 10(b) increases from  $T_w$  at  $y = 0$  to  $T_{\text{sat}}$  at

the interface. The shape of the temperature profile, can be explained with the aid of the simple relation for a turbulent film

$$-q''_{\text{wall}} = k_f \left( 1 + \frac{Pr_f}{Pr_{f,T}} \frac{\epsilon_m}{\nu_f} \right) \frac{dT}{dy}, \quad (20)$$

which assumes the heat flux at the wall is conserved across the film. The term  $Pr_{f,T}$  in Eq. (20) is the turbulent Prandtl number across the film, whose magnitude is close to unity. Since the left hand side of Eq. (20) is constant, the temperature gradient must decrease with increasing  $\epsilon_m/\nu_f$ . Per Fig. 10(a),  $\epsilon_m/\nu_f$  is very small near both the wall and interface, leading to large temperature gradients in these two regions. On the other hand, large  $\epsilon_m/\nu_f$  in between greatly reduces the temperature gradient in this region. These trends produce a seemingly unusual temperature profile, which resembles the computed profiles in Figs. 6(b) and 9(a)–(d).

#### 4.3. Void fraction results

Fig. 11(a) depicts computed void fraction contour plots for FC-72 mass flow rates of  $G = 184.6$  and  $413.0 \text{ kg/m}^2 \text{ s}$ , the lowest and highest values considered in this study. Notice that the liquid

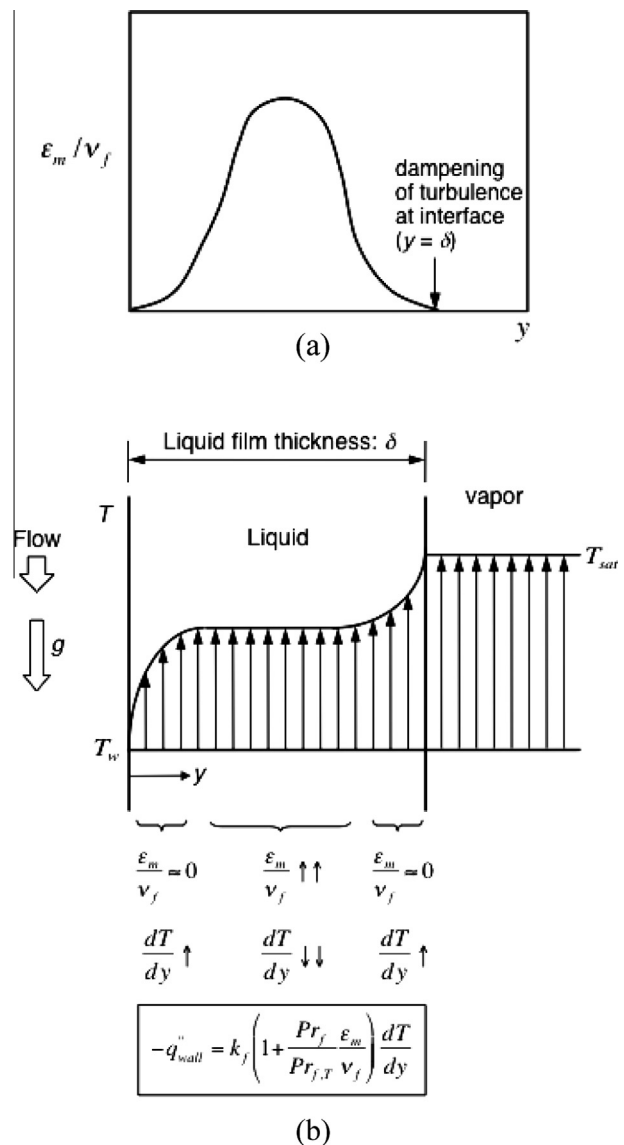


Fig. 10. Schematic representations of (a) eddy momentum diffusivity profile across the liquid film, and (b) influence of eddy momentum diffusivity on temperature profile.

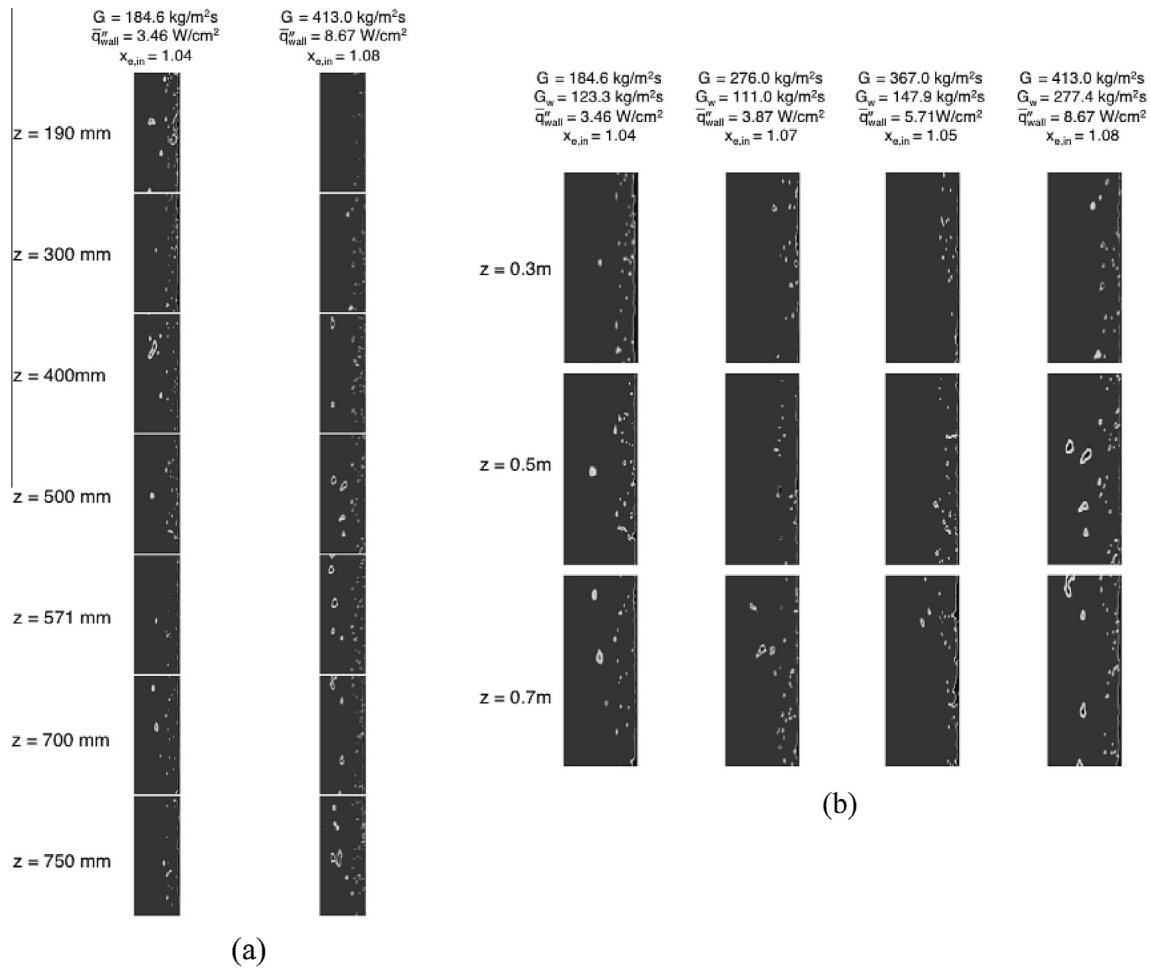


Fig. 11. Computed void fraction contour plots for (a)  $G = 184.6$  and  $413.0 \text{ kg/m}^2 \text{ s}$ , and (b) four FC-72 mass velocities and three axial locations.

film is marred by significant disturbances along with droplet entrainment into the vapor core. Overall, the liquid film thickness increases along flow direction as more vapor is condensed into liquid, and as the vapor velocity and therefore vapor shear exerted on the liquid film gradually abate. There is also an axial increase in the amplitude and wavelength of the interfacial disturbances as suggested in Ref. [20]. The same trends are depicted in Fig. 11(b) for FC-72 mass velocities of  $G = 184.6, 276.0, 367.0$  and  $413.0 \text{ kg/m}^2 \text{ s}$  and three axial locations of  $z = 0.3, 0.5$  and  $0.7 \text{ m}$ .

#### 4.4. Future work

The present findings point to the need to conduct detailed measurements of liquid velocity and liquid thickness to validate future computational models. Such measurements have been conducted in adiabatic falling liquid films [76,77] and provide valuable insight into both turbulence structure and interfacial waviness. However, these measurements are made possible by the relatively large thickness of the liquid film compared to films encountered in condensing flows. As discussed in [78], measurements of liquid velocity in thin layers are possible with the aid of micro-particle image velocimetry ( $\mu$ -PIV), but optical requirements place stringent limits on the size and shape of the flow channel. Given the small thickness of condensing films, better and more miniaturized diagnostic tools are needed to measure liquid layer thickness and characterize interfacial waves [20,25–27,63], as well as temperature profile across the liquid layer [79–82] in non-adiabatic

systems. Only then will detailed validation of computational phase change models be possible. It is also important to note that such diagnostic tools can play a vital role in understanding and computational modeling of far more complex two-phase phenomena, such as the formation of a wavy vapor–liquid wall layer that precedes the formation of critical heat flux (CHF) in flow boiling [83–86].

#### 5. Conclusions

This study involved both experimental and computational investigations of condensation of FC-72 in vertical downflow in a circular tube. An experimental facility was developed to map detailed axial variations of both wall heat flux and wall temperature, which were used to determine axial variations of the condensation heat transfer coefficient. The experimental results were compared to predictions of a two-dimensional, axisymmetric computational model using FLUENT. This paper also provided detailed information on the choice of interfacial phase change model, numerical methods, and convergence criteria. Key findings from the study are as follows.

- (1) The mass transfer intensity factor,  $r_i$ , used in the computational model influences both the condensation heat transfer coefficient and interfacial temperature. Very low  $r_i$  values produce interfacial temperatures far smaller than the



saturation temperature, lower wall temperatures and lower condensation heat transfer coefficients. On the other hand, very high  $r_i$  values produce appreciable interfacial disturbances as well as pose convergence issues. A value of  $r_i = 10,000$  is deemed most suitable for the condensation configuration, working fluid and operating conditions of the present study.

- (2) Overall, the computed condensation heat transfer coefficients show good agreement with experiment, with the highest values encountered in the inlet region where the liquid film is thinnest.
- (3) Eddy momentum diffusivity profiles across the liquid film exhibit appreciable dampening near the interface, which is attributed to turbulence suppression by surface tension forces. The computed eddy diffusivity is zero near the wall and the interface and highest in between.
- (4) The computed temperature profiles across the liquid film exhibit unusual shape, with steep gradients near both the wall and interface, and a mild gradient in between. This shape is shown to be closely associated with the shape of the eddy diffusivity profile.
- (5) Computed void fraction contour plots show a liquid film interface marred by significant disturbances as well as droplet entrainment into the vapor core. The film thickens along the flow direction as more vapor is condensed into liquid and the vapor velocity and vapor shear exerted on the interface gradually abate. Also, both the amplitude and wavelength of the interfacial disturbances increase in the flow direction.
- (6) The findings from the present study point to the need for future, more sophisticated measurements of liquid film thickness, and both velocity and temperature profiles, to both validate and refine computational phase change models.

### Conflict of interest

None declared.

### Acknowledgment

The authors are grateful for the partial support of the National Aeronautics and Space Administration (NASA) under Grant no. NNX13AB01G.

### References

- [1] P.J. Marto, V.J. Lepere, Pool boiling heat transfer from enhanced surfaces to dielectric fluids, *J. Heat Transfer – Trans. ASME* 104 (1982) 292–299.
- [2] W. Nakayama, T. Nakajima, S. Hirasawa, Heat sink studs having enhanced boiling surfaces for cooling of microelectronic components, *ASME Paper* 84-WA/HT-89, 1984.
- [3] T.M. Anderson, I. Mudawar, Microelectronic cooling by enhanced pool boiling of a dielectric fluorocarbon liquid, *J. Heat Transfer – Trans. ASME* 111 (1989) 752–759.
- [4] M.B. Bowers, I. Mudawar, High flux boiling in low flow rate, low pressure drop mini-channel and micro-channel heat sinks, *Int. J. Heat Mass Transfer* 37 (1994) 321–332.
- [5] T.N. Tran, M.W. Wambsganss, D.M. France, Small circular- and rectangular-channel boiling with two refrigerants, *Int. J. Multiphase Flow* 22 (1996) 485–498.
- [6] H.J. Lee, S.Y. Lee, Heat transfer correlation for boiling flows in small rectangular horizontal channels with low aspect ratios, *Int. J. Multiphase Flow* 27 (2001) 2043–2062.
- [7] I. Mudawar, Two-phase micro-channel heat sinks: theory, applications and limitations, *J. Electron. Packag. – Trans. ASME* 133 (2011). 041002-2.
- [8] Y. Katto, M. Kunihiro, Study of the mechanism of burn-out in boiling system of high burn-out heat flux, *Bull. JSME* 16 (1973) 1357–1366.
- [9] M. Monde, T. Inoue, Critical heat flux in saturated forced convective boiling on a heated disk with multiple impinging jets, *J. Heat Transfer – Trans. ASME* 113 (1991) 722–727.
- [10] M.E. Johns, I. Mudawar, An ultra-high power two-phase jet-impingement avionic clamshell module, *J. Electron. Packag. – Trans. ASME* 118 (1996) 264–270.
- [11] L. Lin, R. Ponnappan, Heat transfer characteristics of spray cooling in a closed loop, *Int. J. Heat Mass Transfer* 46 (2003) 3737–3746.
- [12] M. Visaria, I. Mudawar, Theoretical and experimental study of the effects of spray orientation on two-phase spray cooling and critical heat flux, *Int. J. Heat Mass Transfer* 51 (2008) 2398–2410.
- [13] M.K. Sung, I. Mudawar, Experimental and numerical investigation of single-phase heat transfer using a hybrid jet-impingement/micro-channel cooling scheme, *Int. J. Heat Mass Transfer* 49 (2006) 682–694.
- [14] M.K. Sung, I. Mudawar, Correlation of critical heat flux in hybrid jet impingement/micro-channel cooling scheme, *Int. J. Heat Mass Transfer* 49 (2006) 2663–2672.
- [15] M.K. Sung, I. Mudawar, Single-phase and two-phase hybrid cooling scheme for high-heat-flux thermal management of defense electronics, *J. Electron. Packag. Trans. ASME* 131 (2009) 021013.
- [16] I. Mudawar, M.B. Bowers, Ultra-high critical heat flux (CHF) for subcooled water flow boiling – I. CHF data and parametric effects for small diameter tubes, *Int. J. Heat Mass Transfer* 42 (1999) 1405–1428.
- [17] D.D. Hall, I. Mudawar, Ultra-high critical heat flux (CHF) for subcooled water flow boiling – II. High-CHF database and design parameters, *Int. J. Heat Mass Transfer* 42 (1999) 1429–1456.
- [18] M.K. Dobson, J.C. Chato, Condensation in smooth horizontal tubes, *J. Heat Transfer – Trans. ASME* 120 (1998) 193–213.
- [19] A. Cavallini, G. Censi, D.D. Col, L. Doretti, G.A. Longo, L. Rossetto, Condensation of halogenated refrigerants inside smooth tubes, *HVAC&R Res.* 8 (2002) 429–451.
- [20] H. Lee, I. Mudawar, M.M. Hasan, Flow condensation in horizontal tubes, *Int. J. Heat Mass Transfer* 66 (2013) 31–45.
- [21] A. Cavallini, R. Zecchin, A dimensionless correlation for heat transfer in forced convection condensation, in: *Proc. 5th Int. Heat Transfer Conf.*, vol. 3, Tokyo, Japan, 1974, pp. 309–313.
- [22] H. Muller-Steinhagen, K. Heck, A simple friction pressure drop correlation for two-phase flow in pipes, *Chem. Eng. Process.* 20 (1986) 297–308.
- [23] M. Zhang, R.L. Webb, Correlation of two-phase friction for refrigerants in small-diameter tubes, *Exp. Therm. Fluid Sci.* 25 (2001) 131–139.
- [24] S.M. Kim, I. Mudawar, Theoretical model for annular flow condensation in rectangular micro-channels, *Int. J. Heat Mass Transfer* 55 (2012) 958–970.
- [25] I. Park, S.M. Kim, I. Mudawar, Experimental measurement and modeling of downflow condensation in a circular tube, *Int. J. Heat Mass Transfer* 57 (2013) 567–581.
- [26] I. Park, I. Mudawar, Climbing film, flooding and falling film behavior in upflow condensation in tubes, *Int. J. Heat Mass Transfer* 65 (2013) 44–61.
- [27] H. Lee, I. Park, C. Konishi, I. Mudawar, R.I. May, J.R. Juergens, J.D. Wagner, N.R. Hall, H.K. Nahra, M.M. Hasan, J.R. Mackey, Experimental investigation of flow condensation in microgravity, *J. Heat Transfer – Trans. ASME* 136 (2014) 021502.
- [28] R.A. Gingold, J.J. Monaghan, Smoothed particle hydrodynamics: theory and application to non-spherical stars, *Mon. Notices R. Astron. Soc.* 181 (1977) 375–389.
- [29] L.B. Lucy, A numerical approach to the testing of the fission hypothesis, *Astron. J.* 82 (1977) 1013–1024.
- [30] F.H. Harlow, A machine Calculation method for hydrodynamic problems, Los Alamos Scientific Laboratory Report LAMS-1956, New Mexico, 1955.
- [31] S. Osher, J.A. Sethian, Fronts propagating with curvature dependent speed: algorithms based on Hamilton–Jacobi formulations, *J. Comput. Phys.* 79 (1988) 12–49.
- [32] C.W. Hirt, B.D. Nichols, Volume of fluid (VOF) method for the dynamics of free boundary, *J. Comput. Phys.* 39 (1981) 201–225.
- [33] G. Son, V.K. Dhir, Numerical simulation of film boiling near critical pressures with a level set method, *J. Heat Transfer – Trans. ASME* 120 (1998) 183–192.
- [34] M. Sussman, E.G. Puckett, A coupled level set and volume-of-fluid method for computing 3D and axisymmetric incompressible two-phase flows, *J. Comput. Phys.* 162 (2000) 301–337.
- [35] D. Enright, R. Fedkiw, J. Ferziger, I. Mitchell, A hybrid particle level set method for improved interface capturing, *J. Comput. Phys.* 183 (2002) 83–116.
- [36] G. Tomar, G. Biswas, A. Sharma, A. Agrawal, Numerical simulation of bubble growth in film boiling using a coupled level-set and volume-of-fluid method, *Phys. Fluids* 17 (2005) 112103.
- [37] S.O. Unverdi, G. Tryggvason, A front-tracking method for viscous, incompressible, multi-fluid flows, *J. Comput. Phys.* 100 (1992) 25–37.
- [38] G. Tryggvason, B. Bunner, A. Esmaeili, D. Juric, N. Al-Rawahi, W. Tauber, J. Han, S. Nas, Y.-J. Jan, A front-tracking method for the computations of multiphase flow, *J. Comput. Phys.* 169 (2001) 708–759.
- [39] F. Gibou, L. Chen, D. Nguyen, S. Banerjee, A level set based sharp interface method for the multiphase incompressible Navier–Stokes equations with phase change, *J. Comput. Phys.* 222 (2007) 536–555.
- [40] F. Bazdidi-Tehrani, S. Zaman, Two-phase heat transfer on an isothermal vertical surface. A numerical simulation, *Int. J. Heat Fluid Flow* 23 (2002) 308–316.
- [41] H. Ganapathy, A. Shooshtari, K. Choo, S. Dessiatoun, M. Alshehhi, M. Ohadi, Volume of fluid-based numerical modeling of condensation heat transfer and fluid flow characteristics in microchannels, *Int. J. Heat Mass Transfer* 65 (2013) 62–72.

- [42] D.-L. Sun, J.-L. Xu, L. Wang, Development of a vapor–liquid phase change model for volume-of-fluid method in FLUENT, *Int. Commun. Heat Mass Transfer* 39 (2012) 1101–1106.
- [43] R.W. Schrage, *A Theoretical Study of Interphase Mass Transfer*, Columbia University Press, New York, 1953.
- [44] M. Knudsen, *The kinetic theory of gases. Some modern aspects*, Methuen's Monographs on Physical Subjects, London, UK, 1934.
- [45] R. Marek, J. Straub, Analysis of the evaporation coefficient and the condensation coefficient of water, *Int. J. Heat Mass Transfer* 44 (2001) 39–53.
- [46] S. Hardt, F. Wondra, Evaporation model for interfacial flows based on a continuum-field representation of the source terms, *J. Comput. Phys.* 227 (2008) 5871–5895.
- [47] M. Magnini, B. Pulvirenti, J.R. Thome, Numerical investigation of hydrodynamics and heat transfer of elongated bubbles during flow boiling in a microchannel, *Int. J. Heat Mass Transfer* 59 (2013) 451–471.
- [48] J.W. Rose, On interphase matter transfer, the condensation coefficient and dropwise condensation, *Proc. R. Soc. London A* 411 (1987) 305–311.
- [49] O. Kartuzova, M. Kassemi, Modeling interfacial turbulent heat transfer during ventless pressurization of a large scale cryogenic storage tank in microgravity, in: 47th AIAA/ASME/SAE/ASEE Joint Propulsion Conf. & Exhibit, San Diego, CA, 2011.
- [50] I. Tanasawa, Advances in condensation heat transfer, in: J.P. Hartnett, T.F. Irvine (Eds.), *Advances in Heat Transfer*, Academic Press, San Diego, CA, 1991.
- [51] W.H. Lee, A pressure iteration scheme for two-phase flow modeling, in: T.N. Veziroglu (Ed.), *Multiphase Transport Fundamentals, Reactor Safety, Applications*, vol. 1, Hemisphere Publishing, Washington, DC, 1980.
- [52] H.L. Wu, X.F. Peng, P. Ye, Y. Gong, Simulation of refrigerant flow boiling in serpentine tubes, *Int. J. Heat Mass Transfer* 50 (2007) 1186–1195.
- [53] S.C.K. De Schepper, G.J. Heynderichx, G.B. Marin, Modeling the evaporation of a hydrocarbon feedstock in the convection section of a steam cracker, *Comput. Chem. Eng.* 33 (2009) 122–132.
- [54] A. Alizadehdakhel, M. Rahimi, A.A. Alsairafi, CFD modeling of flow and heat transfer in a thermosyphon, *Int. Commun. Heat Mass Transfer* 37 (2010) 312–318.
- [55] Z. Yang, X.F. Peng, P. Ye, Numerical and experimental investigation of two phase flow during boiling in a coiled tube, *Int. J. Heat Mass Transfer* 51 (2008) 1003–1016.
- [56] C. Fang, M. David, A. Rogacs, K. Goodson, Volume of fluid simulation of boiling two-phase flow in a vapor-venting microchannel, *Frontiers Heat Mass Transfer* 1 (2010) 1–11.
- [57] E. Da Riva, D. Del Col, Effect of gravity during condensation of R134a in a circular minichannel, *J. Microgravity Sci. Technol.* 23 (2011) 87–97.
- [58] S. Chen, Z. Yang, Y. Duan, Y. Chen, D. Wu, Simulation of condensation flow in a rectangular microchannel, *Chem. Eng. Process.: Process Intensification* 76 (2014) 60–69.
- [59] B.A. Nichita, J.R. Thome, A level set method and a heat transfer model implemented into FLUENT for modeling of microscale two phase flows, in: AVT-178 Specialists' Meeting on System Level Thermal Management for Enhanced Platform Efficiency, Bucharest, Romania, 2010.
- [60] E.O. Doro, Computational modeling of falling liquid film free surface evaporation (Ph.D. thesis), Georgia Institute of Technology, Atlanta, GA, 2012.
- [61] R. Ranjan, J.Y. Murthy, S.V. Garimella, A microscale model for thin-film evaporation in capillary wick structures, *Int. J. Heat Mass Transfer* 54 (2011) 169–179.
- [62] ANSYS FLUENT 12.1 in Workbench User's Guide, ANSYS Inc., Canonsburg, PA, 2009.
- [63] H. Lee, I. Mudawar, M.M. Hasan, Experimental and theoretical investigation of annular flow condensation in microgravity, *Int. J. Heat Mass Transfer* 61 (2013) 293–309.
- [64] F.R. Menter, Two-equation eddy-viscosity turbulence models for engineering applications, *AIAA J.* 32 (1994) 1598–1605.
- [65] T.H. Shih, W.W. Liou, A. Shabbir, Z. Yang, J. Zhu, A new  $k-\epsilon$  eddy-viscosity model for high Reynolds number turbulent flows: model development and validation, *Comput. Fluids* 24 (1995) 227–238.
- [66] N. Mascarenhas, I. Mudawar, Investigation of eddy diffusivity and heat transfer coefficient for free-falling turbulent liquid films subjected to sensible heating, *Int. J. Heat Mass Transfer* 64 (2013) 647–660.
- [67] N. Mascarenhas, I. Mudawar, Study of the influence of interfacial waves on heat transfer in turbulent falling films, *Int. J. Heat Mass Transfer* 67 (2013) 1106–1121.
- [68] J.U. Brackbill, D.B. Kothe, C. Zemach, A continuum method for modeling surface tension, *J. Comput. Phys.* 100 (1992) 335–354.
- [69] R.I. Issa, Solution of the implicitly discretized fluid flow equations by operator splitting, *J. Comput. Phys.* 62 (1985) 40–65.
- [70] B. van Leer, Towards the ultimate conservative difference scheme, V. A second order sequel to Godunov's method, *J. Comput. Phys.* 32 (1979) 101–136.
- [71] B.P. Leonard, Stable and accurate convective modelling procedure based on quadratic upstream interpolation, *Comput. Methods Appl. Mech. Eng.* 19 (1979) 59–98.
- [72] D.L. Youngs, Time-dependent multi-material flow with large fluid distortion, in: *Numerical Methods Fluid Dynamics*, Academic Press, New York, 1982.
- [73] S.V. Patankar, *Numerical Heat Transfer and Fluid Flow*, Hemisphere Publishing, New York, 1980.
- [74] MATLAB Curve Fitting Toolbox 1: user's guide, Mathworks, Natick, MA, 2006.
- [75] I. Mudawar, M.A. El-Masri, Momentum and heat transfer across freely-falling turbulent liquid films, *Int. J. Multiphase Flow* 12 (1986) 771–790.
- [76] I. Mudawar, R.A. Houpt, Mass and momentum transport in smooth falling liquid films laminarized at relatively high Reynolds numbers, *Int. J. Heat Mass Transfer* 36 (1993) 3437–3448.
- [77] I. Mudawar, R.A. Houpt, Measurement of mass and momentum transport in wavy-laminar falling liquid films, *Int. J. Heat Mass Transfer* 36 (1993) 4151–4162.
- [78] W. Qu, I. Mudawar, S.-Y. Lee, S.T. Wereley, Experimental and computational investigation of flow development and pressure drop in a rectangular micro-channel, *J. Electron. Packag.* – Trans. ASME 128 (2006) 1–9.
- [79] J.A. Shmerler, I. Mudawar, Local heat transfer coefficient in wavy free-falling turbulent liquid films undergoing uniform sensible heating, *Int. J. Heat Mass Transfer* 31 (1988) 67–77.
- [80] J.A. Shmerler, I. Mudawar, Local evaporative heat transfer coefficient in turbulent free-falling liquid films, *Int. J. Heat Mass Transfer* 31 (1988) 731–742.
- [81] T.H. Lyu, I. Mudawar, Statistical investigation of the relationship between interfacial waviness and sensible heat transfer to a falling liquid film, *Int. J. Heat Mass Transfer* 34 (1991) 1451–1464.
- [82] T.H. Lyu, I. Mudawar, Determination of wave-induced fluctuations of wall temperature and convective heat transfer coefficient in the heating of a turbulent falling liquid film, *Int. J. Heat Mass Transfer* 34 (1991) 2521–2534.
- [83] C.O. Gersey, I. Mudawar, Effects of heater length and orientation on the trigger mechanism for near-saturated flow boiling critical heat flux – I. Photographic study and statistical characterization of the near-wall interfacial features, *Int. J. Heat Mass Transfer* 38 (1995) 629–641.
- [84] C.O. Gersey, I. Mudawar, Effects of heater length and orientation on the trigger mechanism for near-saturated flow boiling critical heat flux – II. Critical heat flux model, *Int. J. Heat Mass Transfer* 38 (1995) 643–654.
- [85] J.C. Sturgis, I. Mudawar, Critical heat flux in a long, rectangular channel subjected to onedirectional heating – I. Flow visualization, *Int. J. Heat Mass Transfer* 42 (1999) 1835–1847.
- [86] J.C. Sturgis, I. Mudawar, Critical heat flux in a long, rectangular channel subjected to onedirectional heating – II. Analysis of critical heat flux data, *Int. J. Heat Mass Transfer* 42 (1999) 1849–1862.